

Features in cosmic-ray lepton data unveil the properties of nearby cosmic accelerators

O. Fornieri,^{a,b,c,1} D. Gaggero^c and D. Grasso^b

^aDepartment of Physical Sciences, Earth and Environment, University of Siena,
Via Roma 56, 53100 Siena, Italy

^bINFN Sezione di Pisa,
Polo Fibonacci, Largo B. Pontecorvo 3, 56127 Pisa, Italy

^cInstituto de Física Teórica UAM-CSIC,
Campus de Cantoblanco, E-28049 Madrid, Spain

E-mail: ottavio.fornieri@pi.infn.it, daniele.gaggero@uam.es, dario.grasso@pi.infn.it

Abstract. We present a comprehensive discussion about the origin of the features in the leptonic component of the cosmic-ray spectrum. Working in the framework of a up-to-date CR transport scenario tuned on the most recent AMS-02 and Voyager data, we show that the prominent features recently found in the positron and in the all-electron spectra by several experiments are explained in a scenario in which pulsar wind nebulae (PWNe) are the dominant sources of the positron flux, and nearby supernova remnants shape the high-energy peak of the electron spectrum. In particular we argue that the drop-off in positron spectrum found by AMS-02 at ~ 300 GeV can be explained — under different assumptions — in terms of a prominent PWN that provides the bulk of the observed positrons in the ~ 100 GeV domain, on top of the contribution from a large number of older objects. Finally, we turn our attention to the spectral softening at ~ 1 TeV in the all-lepton spectrum, recently reported by several experiments, showing that it requires the presence of a nearby supernova remnant at its final stage.

¹Corresponding author.

Contents

1	Introduction	1
2	Characterization of the large-scale CR transport scenario	3
2.1	Description of the setup	3
2.2	Setting source and transport parameters against CR nuclei data	4
2.3	Primary electrons and secondary positrons	5
3	The positron excess	6
3.1	Setting the stage: basic aspects of pulsar acceleration in pulsar wind nebulae and relevant caveats	6
3.2	Diffusive propagation of leptons in the Galaxy: study of the analytical solution	8
3.3	The contribution from old and young pulsars to the positron flux	10
3.4	Characterization of the high-energy flux	11
4	Local electron accelerators explain the high-energy electron data	13
4.1	Contribution from the known objects	14
4.2	Characterization of a potential source reproducing the ~ 1 TeV break	16
5	Conclusions	17
A	Single-source solution to the transport equation	20
B	Posterior distribution functions for the fit to the positron flux	22
C	Estimation of the release time from PWNe	22
D	Notes on the pulsars from ATNF Catalogue	23

1 Introduction

The origin and transport properties of leptonic cosmic rays (CRs) have intrigued scientists for decades. Differently from the nuclear components of CRs, the propagation of CR leptons in the interstellar medium (ISM) of the Galaxy is characterized not only by a diffusive propagation but also by strong energy losses which — above few GeV — are dominated by synchrotron emission and Inverse Compton (IC) scattering.

Those losses, that are at work both during the acceleration process in the source environment and the propagation in the ISM, are likely to be responsible for the steeper spectrum observed for CR electrons with respect to that of CR hadrons, as well as of its lower maximal energy. Furthermore, the transition from a diffusion-dominated to loss-dominated regime in the ISM is expected to produce a cooling break in the propagated spectrum of CR leptons.

The accurate measurement of such features in the CR lepton spectrum — which may be observed either directly at Earth or indirectly by looking for its imprint on the synchrotron and IC diffuse emission spectra — may offer valuable clues on the source ages/positions as well as on the details of CR transport. Moreover, given the $\propto E^2$ scaling of the leptonic energy-loss rate, the effective *horizon* associated to CR leptons progressively shrinks with

increasing energy, hence the stochastic nature of the sources is expected to play a more and more important role with increasing energy. This trend implies even more pronounced features at high energies, as noticed already in [1] and further elaborated in more recent times [2, 3].

On the experimental side, several experiments have recently provided accurate measurement of the electrons or electron+positrons spectrum up to $\sim \mathcal{O}(10)$ TeV and have revealed several features. It is therefore challenging to connect these observed features to the physics arguments explained above.

Regarding the electron spectrum, we remark in particular that the AMS-02 e^- spectrum exhibits a hardening at $\simeq 40$ GeV [4]. At even higher energies, H.E.S.S. [5, 6], DAMPE [7] and CALET [8] measured the $e^- + e^+$ spectrum up to $\simeq 20$ TeV and outlined a sharp softening at $\simeq 1$ TeV. Above that feature, the power-law spectrum extends with no clear sign of cutoff all the way up to the maximal detected energy.

Another valuable piece of information comes from the spectrum of CR positrons. A guaranteed flux of e^+ is expected due to the interaction of CR nuclei (mainly protons and Helium) with the ISM gas. This component is expected to decrease with respect to the $e^- + e^+$ flux with increasing energy. However, the discovery of an increasing positron fraction above 10 GeV by PAMELA [9], later confirmed and better characterized by AMS-02 [10], was then corroborated by the measurement of the absolute e^+ spectrum by both experiments [11, 12] showing that the anomaly cannot be attributed to a steeper-than-expected e^- spectrum and that a primary origin of Galactic high-energy positrons needs to be identified. More recently, the AMS-02 Collaboration provided a clear evidence of a cutoff in the e^+ spectrum at about ~ 300 GeV [13] which may shed light on the nature of their source(s) and is not expected in alternative transport scenarios where CR positrons are entirely interpreted as secondaries of CR nuclei [14].

In this paper we investigate whether nearby and relatively young cosmic accelerators such as supernova remnants (SNRs) — which can accelerate high-energy hadrons and electrons via diffusive shock acceleration [15–18] — and pulsar wind nebulae (PWNe) — which are expected to be symmetric electron+positron pairs emitters [19, 20] — can explain those experimental results in the context of a large-scale CR transport setup tuned on the most updated CR nuclei data.

We notice that a scenario invoking PWNe as the origin of the positron excess has recently received further support from the detection of TeV γ -ray halos around the Geminga and Monogem nearby pulsars by HAWC [21] and by Fermi-LAT [22], which has been interpreted in terms of IC emission from a fresh population of electrons and, plausibly, positrons [23].

The structure of the paper is the following. We first identify a transport scenario that provides a satisfactory description of light nuclei CR data released by AMS-02 mostly and which is required to fix the diffusion parameters which enter in determining the shape and the features in the propagated lepton spectra. Then, we turn our attention to the positron flux and model its observed spectrum and its features in terms of a conventional secondary component produced by hadronic spallation, a primary extra component that dominates at intermediate energies and originates by a large number of distant, old pulsars, plus one or few nearby pulsars as the main possible contributor at high-energies. Finally, we concentrate on the electron and all-lepton data and analyze the contributions from nearby asymmetric accelerators within the same transport scenario.

2 Characterization of the large-scale CR transport scenario

In this section we settle the CR transport setup that will be adopted throughout the paper. It is understood that this setup captures an effective large-scale average of CR transport properties and does not account for strong local fluctuations, as those pointed out for instance in [21]. We will show *a posteriori* that the presence of those regions of very effective confinement does not significantly affect the results of our analysis.

2.1 Description of the setup

The usual starting point is the phenomenological equation that captures CR diffusion in space and momentum, energy losses, advection, reacceleration, nuclear spallation and decays [24, 25]:

$$-\tilde{\nabla} \cdot (D\tilde{\nabla} N_i + \vec{v}_w N_i) + \frac{\partial}{\partial p} \left[p^2 D_{pp} \frac{\partial}{\partial p} \left(\frac{N_i}{p^2} \right) \right] - \frac{\partial}{\partial p} \left[\dot{p} N_i - \frac{p}{3} (\tilde{\nabla} \cdot \vec{v}_w) N_i \right] = Q + \sum_{i < j} \left(c\beta n_{\text{gas}} \sigma_{j \rightarrow i} + \frac{1}{\gamma \tau_{j \rightarrow i}} \right) N_j - \left(c\beta n_{\text{gas}} \sigma_i + \frac{1}{\gamma \tau_i} \right) N_i \quad (2.1)$$

The equation is solved for all the relevant species with DRAGON [26, 27], and the following settings are specified:

- As far as CR nuclei (and protons) are concerned, we adopt a continuous source distribution in two dimensions — cylindrical symmetry — taken from [28]. Such distribution accounts for the spatial distribution of both type Ia (traced by old disk stars), and type II (traced by pulsars) supernovae.

The injection spectrum for each species is modeled as a broken power-law in rigidity. Two breaks are introduced to effectively reproduce low-energy data as well as the hardening measured by AMS-02 and other experiments at few hundred GeV/n¹.

- For the aim of this study we assume uniform and isotropic CR diffusion characterized by a spatially-independent scalar diffusion coefficient that exhibits the following scaling as a function of rigidity:

$$D_{xx}(p) = D_0 \left(\frac{p}{p_0} \right)^\delta \quad (2.2)$$

where $D_0 \equiv D(p_0)$ is the diffusion coefficient normalization at a reference rigidity, that in this work we fix to be $p_0 = 1$ GV.

- We account for diffusive reacceleration adopting a finite value of the Alfvén velocity v_A which fixes the diffusion coefficient in momentum space through the expression [25, 29]

$$D_{pp}(p) = \frac{v_A^2 p^2}{\delta(4 - \delta)(4 - \delta^2) D_{xx}(p)}. \quad (2.3)$$

¹Although this features is likely due to CR diffusion as suggested by the stronger hardening found by AMS-02 for secondary nuclei, for the aims of this study our approach is equivalent to introducing a break in the diffusion coefficient.

	v_A [km/s]	D_0 [m ² /s]	δ	$\Gamma_{\text{inj,L}}$	$\rho_{b,1}$ [GV]	$\Gamma_{\text{inj,M}}$	$\rho_{b,2}$ [GV]	$\Gamma_{\text{inj,H}}$
p	13	$1.98 \cdot 10^{24}$	0.45	1.8	7	2.4	335	2.26
He				2.0		2.28	165	2.15
C				2.0		2.38	165	2.15
O				2.0		2.38	165	2.15

Table 1: The values of the main source and propagation parameters characterizing our reference transport model are reported in this table.

- The hadronic energy losses (ionization and Coulomb scattering) are naturally taken into account in the standard DRAGON implementation. Bremsstrahlung, synchrotron and Inverse Compton losses are also considered for leptons, as implemented in the public DRAGON code.

The astrophysical ingredients relevant for the computation of the energy-loss term are the following:

- A smooth, cylindrically symmetric gas distribution, taken from [30, 31] and implemented in the standard public version of both GALPROP [32–34] and DRAGON.
- The magnetic field, parametrized as in [35]; given that parametrization, we set $B_{0,\text{disk}} = 2 \mu\text{G}$, $B_{0,\text{Halo}} = 4 \mu\text{G}$ and $B_{0,\text{turb}} = 7.5 \mu\text{G}$.
- Concerning the spallation ($\sigma_{i \rightarrow j}$) and inelastic scattering (σ_i) cross-sections, in order to allow a more direct comparison with most of the related literature we use the routines implemented in the standard public version of GALPROP [33, 34] (see however [36] for an alternative compilation).

2.2 Setting source and transport parameters against CR nuclei data

While gas density, magnetic and interstellar radiation field distributions are fixed (though with some uncertainties) on the basis of astronomical data, CR injection spectra and diffusion parameters are largely unknown and have to be settled by comparing DRAGON predictions with CR data. We use here AMS-02 data for almost all species and the B/C ratio (see references in the caption of Figure 1) complemented with Voyager data for low-energy protons and other nuclei outside the Heliosphere (unmodulated), and HEAO-3 [37] to determine the normalization of nuclear species heavier than Nitrogen.

We performed a multi-dimensional grid of DRAGON runs and identify a satisfactory scenario, characterized by the parameters listed in Table 1.

It should be noted that an approximate degeneracy holds between the diffusion coefficient normalization and the diffusive halo height scale H since the CR escape time, hence the secondary/primary ratio, only depends on the ratio D_0/H . In this paper we use $H = 4$ kpc.

As shown in Figures 1a and 1b, the observed spectra are reproduced introducing a low-energy break at 7 GeV/n, for all species, and a high-energy hardening at 335(165) GeV/n for protons (heavier nuclei).

Similarly to the results reported in [44], and — more recently — in [45, 46], the B/C ratio is nicely matched for a value of δ close to 0.45. Performing a statistical analysis aimed

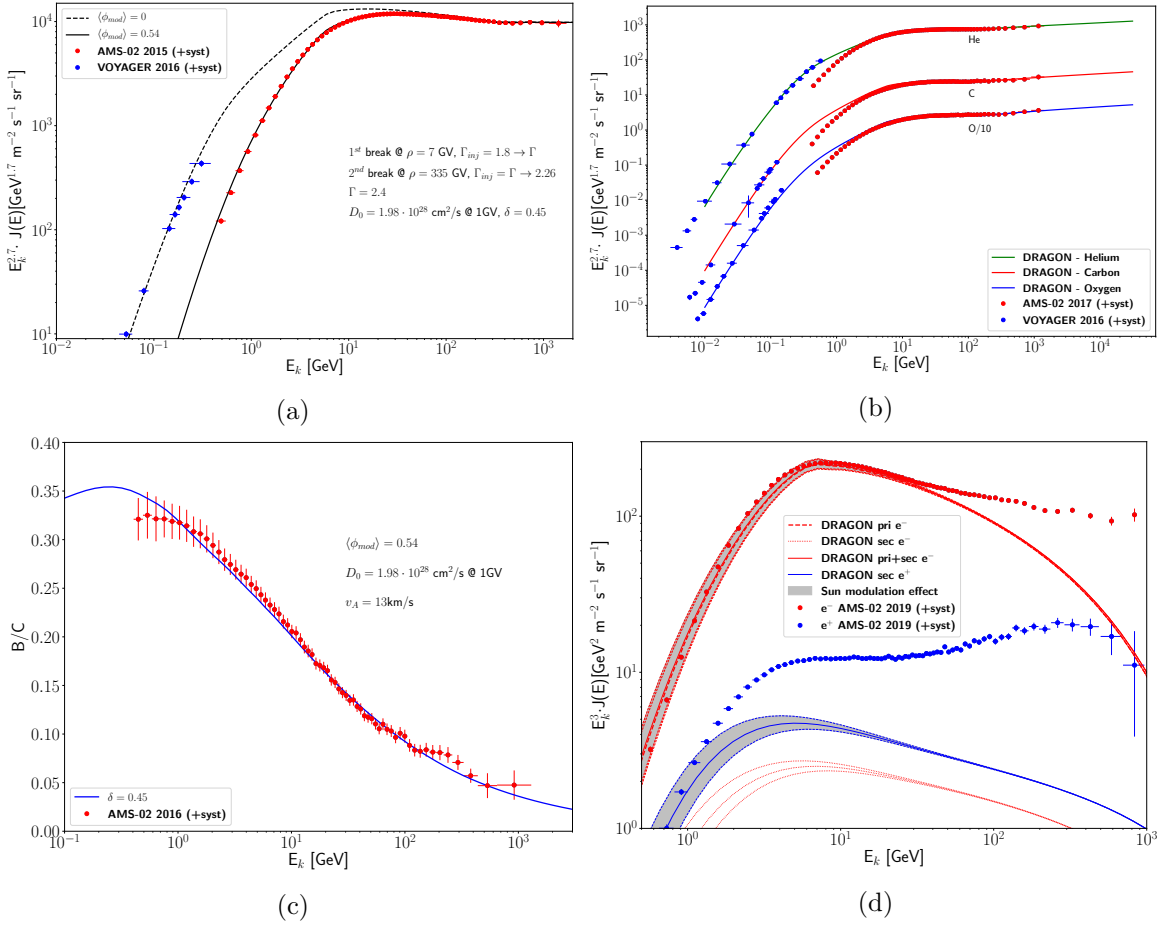


Figure 1: The propagated spectra computed with our reference model of (a) protons, (b) Helium, Carbon and Oxygen (Oxygen flux is divided by 10 for clarity) are compared with AMS-02 [38, 39] (accounting for solar modulation) and Voyager [40] (interstellar) data. In (c) the B/C ratio is computed for the same model and is plotted against AMS-02 experimental data [41]. (d) Primary and secondary production of electrons and positrons, computed with DRAGON. The red and blue dots are AMS-02 experimental data [4, 13]. The silver band accounts for the solar modulation $\langle\phi_{mod}\rangle = 0.54 \pm 0.10$, estimated according to [42, 43] for the whole period of data taking.

at the determination of the uncertainties on the propagation parameters is beyond the aims of this work. We notice however that varying the main parameters in the small allowed ranges found in [46] would have no relevant impact on the electron and positron spectra and the conclusions of this work.

2.3 Primary electrons and secondary positrons

In the standard CR transport scenario, the Galactic SNRs are expected to generate the bulk of the observed CR electrons as well. Moreover, a guaranteed source of secondary electrons and positrons is provided by the scattering of CR nuclei — mostly protons and ^4He — with the ISM gas.

As far as the primary electrons are concerned, we remark that, although the acceleration mechanism is expected to be the same as the one at work for the nuclear species, the injection spectrum into the ISM should be steeper (with $\Delta\Gamma$ as large as up to ~ 0.4) due to synchrotron

losses in the SNR magnetic field, which is also amplified by CR-induced turbulence [47]. Moreover, as shown in [48], the spiral pattern induces an extra steepening because of the enhanced energy losses experienced by the leptonic component due to the larger average distance of the sources from Earth.

Therefore, we compute the propagated spectra at Earth with DRAGON adopting the setup derived in the previous paragraph and implementing an electron injection spectrum $\Gamma_{\text{inj}}^e = 2.7$ (1.6) above (below) 7 GeV. The result is shown in Figure 1d. We notice that the DRAGON output is in good agreement with analytical computations [14, 49] predicting a propagated spectral index $\Gamma = \Gamma_{\text{inj}} + \frac{\delta}{2} + \frac{1}{2}$ above few GeV.

The AMS-02 e^- are well reproduced up to ~ 50 GeV, where the measured spectrum displays a clear hardening (see Figure 1d).

That feature corresponds to the expected breakdown of the assumption of a continuous, steady-state source term that characterizes the large-scale models developed with DRAGON. Indeed, the mean distance between active SNRs is expected to be of few kpc's. As a consequence, we expect that already above ~ 100 GeV the energy losses will limit the number of SNRs contributing to the observed CR electron flux to just a few. The contribution of individual CR electron sources will be discussed in detail in Section 4.

As far as the secondary positrons are concerned, we compute the propagated spectrum at Earth with DRAGON within the same transport setup. The result is also shown in Figure 1d. Similarly to what was already pointed out with the first release of the PAMELA data [50], we find that above few GeV this component is much steeper than expected, hence cannot reproduce the data.

Even though alternative CR propagation scenarios may be invoked to account for the unexpected production of positrons [51], as well as interpretations based on dark matter annihilation (see for instance the recent review [52] and references therein), lepton pair emission from pulsar wind nebulae seems to be a more natural candidate. We will assess their contribution in the next paragraph.

3 The positron excess

In this section we focus on positron data and present a detailed discussion on their possible interpretations. In particular we address from the phenomenological point of view the role of local and distant sources of relativistic electron+positron pairs, such as pulsar wind nebulae (PWNe): we discuss whether a scenario in which the positron flux is dominated by this class of sources is viable (both from the point of view of the energy budget and of the spectral features) and assess whether the current data allow us to pinpoint which PWNe are most likely to contribute in the different energy ranges.

3.1 Setting the stage: basic aspects of pulsar acceleration in pulsar wind nebulae and relevant caveats

Pulsar wind nebulae are structures found inside the shells of supernova remnants, which emit a broad-band spectrum of non-thermal radiation powered by fast-spinning magnetized neutron stars with a typical radius $R \sim 10$ km and periods of $\mathcal{O}(0.1 - 10)$ s, typically detected in the radio and/or gamma-ray band as *pulsars*.

As mentioned in the Introduction, the role of pulsars and PWNe as relevant and efficient antimatter factories, mostly in the form of electron+positron pairs, and their contribution

to the electron+positron flux detected by space-borne experiments has been discussed for a long time in the literature, since the pioneering works of the past century [1, 53, 54]. We will recall in this section some important aspects of the physics that characterizes these objects in order to motivate our phenomenological parameterization of the problem.

In order to characterize the emission from a PWN, it is important to assess: **1)** the energy release as a function of time, and **2)** the acceleration mechanisms of the electron+positron pairs, hence the energy spectrum of such leptons when they are eventually released in the interstellar medium (ISM).

1. Regarding the former, we recall that the pulsar spin-down is usually described by the following model-independent equation:

$$\dot{\Omega}(t) = -\kappa_0 \cdot \Omega(t)^n, \quad (3.1)$$

where $\Omega(t) = P^{-1}$ is the rotation frequency, κ_0 and n are parameters that depend on the specific energy-loss process; in particular n is commonly called *braking index*.

This equation can be solved to get $\Omega(t)$ and the time evolution of the luminosity, which can be written as follows, in terms of the conversion efficiency (η^\pm) of the released energy into e^\pm pairs:

$$L(t) = I\Omega(t)\dot{\Omega}(t) = \frac{\eta^\pm L_{0,\gamma}}{\left(1 + \frac{t}{\tau_0}\right)^{\frac{n+1}{n-1}}} \quad (3.2)$$

where we defined

$$\tau_0 \equiv \frac{1}{(n-1)\kappa_0\Omega_0^{n-1}}. \quad (3.3)$$

Here, t is the age of the source, provided that the diffusive time ($t^* \equiv t^*(E)$) needed for a particle to travel from the source to the Earth is much smaller than the age itself, which is true for nearby ($d \sim \mathcal{O}(100)$ pc) sources of high-energy leptons ($\mathcal{O}(100)$ GeV).

If the energy loss mechanism that causes the pulsar spin-down is exclusively magnetic dipole emission (MD), the braking index becomes $n = 3$ [55]. In this case, the characteristic timescale of the frequency (and luminosity) drop is given by

$$\tau_0^{\text{MD}} = \frac{3Ic^3}{B^2 R^6 \Omega_0^2} \quad (3.4)$$

where I is the moment of inertia of the spinning neutron star, B is the surface magnetic field, Ω_0 is the initial frequency. However, it is important to point out that the actual measurements of the pulsar braking index are very challenging and available for a limited number of cases only [56], and in each of them the results show values of $1.9 < n < 2.8$, significantly different from the ideal MD model.

It is important to comment about the interplay between the braking index n , the pulsar age and the characteristic energy-loss time τ_0 . Within the magnetic-dipole emission framework, the directly observed quantities P and \dot{P} allow, under the assumption $P_0 \ll P_{\text{current}} \equiv P$, to infer a *characteristic age* of the pulsar [55]:

$$t_{\text{ch}} \approx \frac{P}{(n-1)\dot{P}} = \frac{P}{2\dot{P}}. \quad (3.5)$$

For all the nearby pulsars observed and tabulated in the ATNF catalogue² [57] the ratio between this quantity and the theoretical spin-down decay time given by Equation (3.4) is typically one order of magnitude lower than 1 (~ 0.3), which would allow to approximate (at the very first order) the pulsar energy output as a constant over time, as clearly seen Taylor-expanding (3.2) $L(t) \approx \eta^\pm L_{0,\gamma} (1 - \frac{n+1}{n-1} \cdot t/\tau_0^{\text{MD}})$.

However, this is a model-dependent consideration. Given the large discrepancy between the MD-predicted braking index and the observed ones, other energy-loss mechanisms might be at work, and this leaves us with high uncertainties on the τ_0 parameters, which represents the time evolution of the luminosity function. This parameter could in fact be much smaller than the age of the source, which would allow us to approximate the particle release as instantaneous. Therefore, in the following we will consider the two limiting cases of burst-like injection of particles (discussed many times in the literature) and constant-luminosity injection, in order to bracket the above-mentioned uncertainty.

2. As far as the second aspect is concerned, we recall that the broad-band radiation emitted by PWNe can be typically modeled as synchrotron and IC emission from a population of relativistic electrons and positrons distributed in energy as a broken power-law spectrum. These leptonic pairs, initially extracted by the surface of the neutron star, are then most likely accelerated at, or close to, the termination shock (TS) by a variety of possible mechanisms.

The current data regarding the non-thermal radiation (in *Radio* and *X-ray* frequencies) emitted from several well-observed PWNe [58] require a lepton spectrum which has the shape of a broken power law, with a hard spectrum (with slope $1 \lesssim \Gamma_{\text{inj}} \lesssim 2$) below a break at $\sim 200 - 400$ GeV, and a steeper one ($\Gamma_{\text{inj}} > 2$) at larger energies (see [20, 59–61]). The hard, low-energy spectrum has been object of debate over the years, and several acceleration mechanisms were proposed, including magnetic reconnection at the TS and resonant absorption of ion-cyclotron waves.

In the following, inspired by these considerations, we will adopt both the broken power-law parameterization, and a single power law with exponential cutoff as well, to allow comparison with many previous results (see for instance the recent reviews [52, 62] and the references therein).

As a final remark, we point out that the particles are expected to be released from the PWN region with some delay. This delay is given by the time the pulsar — due to its proper motions — takes to leave the associate SNR shell, which is estimated to be $t_{\text{rel}} \sim 6 \cdot 10^4$ yr for pulsars (see Appendix C). In the same Appendix we will discuss how that value may grow taking into account the results of recent analyses of the HAWC [21] and Fermi-LAT [22] data for the Geminga and Monogem regions, showing that e^\pm diffusion may be delayed around those objects.

3.2 Diffusive propagation of leptons in the Galaxy: study of the analytical solution

With the parametrization of the source term and the delay of the particle release properly settled, we now turn our attention to the propagation of the electron+positron pairs from individual sources in the ISM.

²<http://www.atnf.csiro.au/people/pulsar/psrcat/>

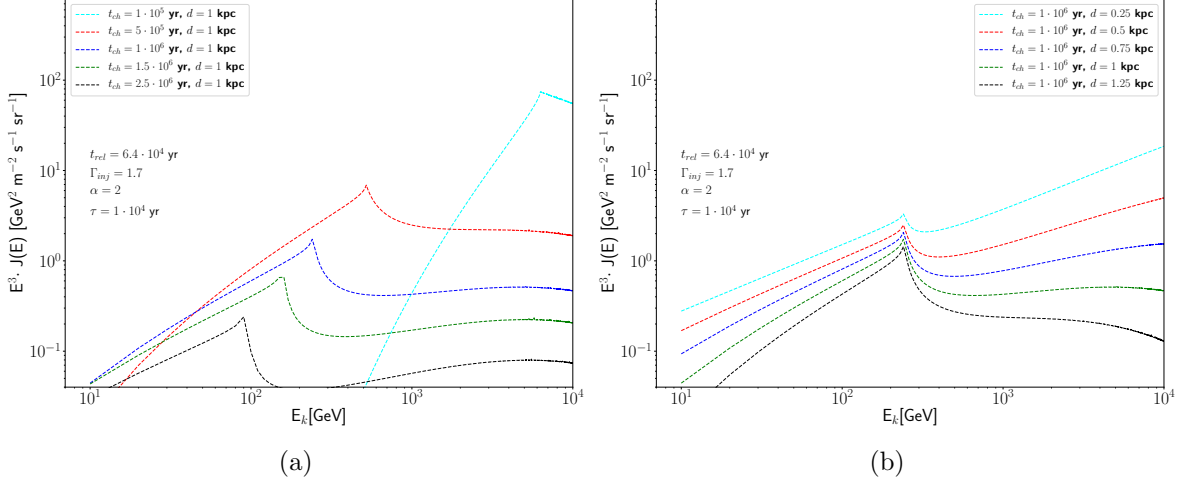


Figure 2: Solution of the transport equation for a decaying-luminosity single-source, plotted for objects of (a) different ages and fixed distance (1 kpc) and (b) different distances and fixed age ($1 \cdot 10^6$ yr). The order of magnitude of the energy-budget is compatible with the one expected from pulsar emission ($\mathcal{O}(10^{47} - 10^{49} \text{ erg})$). The injection index is $\Gamma_{\text{inj}} = 1.7$, although we verified that the shifting is independent of it. It is clear how, for older sources, the emission peak shifts to the low-energy range.

We describe the transport process by means of a simplified version of the equation (2.1) where low-energy effects such as advection and reacceleration are neglected and spherical symmetry is assumed.

Under these assumptions, we can write:

$$\frac{\partial f(E, t, r)}{\partial t} = \frac{D(E)}{r^2} \frac{\partial}{\partial r} r^2 \frac{\partial f}{\partial r} + \frac{\partial}{\partial E} (b(E)f) + Q, \quad (3.6)$$

where $b(E)$ is the energy-loss rate. This term, in general, takes into account a variety of processes (ionization, Coulomb scattering, bremsstrahlung, inverse Compton, synchrotron). While the DRAGON setup accounts for all these loss processes in a spatial-dependent framework, in this section we approximate the energy loss term as

$$\frac{dE}{dt} \simeq -b_0 E^2 \quad (3.7)$$

with $b_0 = 1.4 \cdot 10^{-16} \text{ GeV}^{-1} \text{ s}^{-1}$. This expression captures the dominant leptonic processes (Inverse Compton and synchrotron) in the local environment, as far as the energy range of interest for the present work is concerned ($E > 1 \text{ GeV}$).

Equation (3.6) can be solved analytically [54], as detailed in Appendix A.

For the purpose of this work, we are interested in the behaviour of the solution as a function of the age and distance. A time-decaying luminosity function as the one given in Equation (3.2), assuming a power-law injection spectrum, yields the solutions plotted in Figure 2.

The prominent peak in the solution is due (at fixed distance) to the interplay between the diffusion dominating at low energy and energy losses at high energy. While a burst-like injection gives rise to a sharp cutoff above the peak energy, a long-lasting source results in a plateau or even a growing-with-energy behaviour for large values of τ_0 or short distances.

Taking into account the possible presence of UV cutoff in the source spectrum (see discussion in the previous paragraph), the peak energy is determined by the following condition

$$E_{\max}(t) = \min \left\{ \frac{1}{b_0(t - t_{\text{rel}})}, E_{\text{cut}} \right\}, \quad (3.8)$$

where t is the age of the source and t_{rel} the time it takes for particles to leave the source region. Therefore, the peak progressively shifts towards lower energies for increasing PWN age.

3.3 The contribution from old and young pulsars to the positron flux

We start by considering the low-energy part of the positron spectrum and assume that it is originated by a large number of PWNe with age older than $\sim 10^6$ years.

This assumption is motivated by the trend regarding the peak energy outlined above, and by the fact that, below ~ 100 GeV, the diffusion horizon ($d_{\max} = \sqrt{4D(E)(t - t_{\text{rel}})}$) grows up to few kiloparsecs. Within that distance, a very large number of pulsars are observed, and — provided that the diffusive time of their injected particles is smaller than their ages — all of them are expected to contribute to the flux reaching the Earth, at energies that get lower with increasing age.

The cumulative spectrum of this “large scale” e^\pm component is therefore the convolution of the contributions from many single sources, as discussed in the above, integrated over their age distribution.

A detailed Monte Carlo simulation of this integrated contribution is beyond the scope of this paper and is postponed to a dedicated work. However, we tested the cumulative contribution from a sample of 10^4 pulsars with ages between 10^6 and 10^8 yr (the sample number is compatible with the observed SN rate [63]), assuming that e^\pm pairs are injected from these sources with a total energy budget in the $[10^{46} - 10^{49}]$ erg range, and with spectral indices between 1.3 and 1.9. We found that the simulated total spectrum from those sources displays a small scatter for different realizations of the pulsar distribution and — with good approximation — typically follows a smooth power-law.

Motivated by these considerations, we choose to consider an effective modeling of such large scale e^\pm component within the DRAGON framework, similarly to what done in previous works (see *e.g.* [64]). Therefore, we add to our setup a charge-symmetric smooth ($\Gamma_{\text{extra}} = 2.28$) *extra-component* with the same spatial distribution of SNRs and tune its normalization to AMS-02 data.

We now focus on the high-energy part $E > 100$ GeV of the e^\pm spectrum which should receive a significant contribution either from relatively young pulsars ($t \lesssim 10^5$ years) or even by older pulsars if they are long lived.

The key aspect in this energy domain is the pronounced drop-off in the positron spectrum observed by AMS-02 above ~ 250 GeV. The considerations discussed so far may lead us to two distinct interpretations of this feature:

- Given the properties of the analytical solution, assuming that no relevant spectral steepening or cutoff is present at the source in this energy range, it is possible to ascribe the feature to the interplay between diffusion and energy loss. This would imply a dominant contribution in this range from a number of pulsar wind nebulae of approximate age of $\sim 10^6$ yr (see Figure 2a). Besides, in order to reproduce the above-mentioned drop-off in the data, such PWNe should be at a distance larger than

or, at least, similar to $\sim \sqrt{4 D(E = 230 \text{ GeV}) \cdot (t_{\text{age}} = 10^6 \text{ yr})} \approx 1.5 \text{ kpc}$ (see Figure 2b).

- Alternatively, given our knowledge of the injection spectrum of PWNe, summarized in Section 3.1, a natural interpretation is that the positron flux around 200 GeV is dominated by few (or one) nearby, young pulsar wind nebulae, which provide a relevant contribution on top of the diffuse, large-scale component discussed above, and is characterized by either a spectral break or a cutoff at that energy, explained by the acceleration processes taking place near the termination shock.

Below we will explore the second option leaving a deeper analysis of the first one to a forthcoming work. We just mention that a detailed Monte Carlo simulations was recently performed in [65]³.

3.4 Characterization of the high-energy flux

We here investigate in further details the case where, on top of the secondary positron flux and a large-scale extra component associated to a large number of old PWNe — as discussed in Section 3.3 — the high-energy positron flux is dominated by the contribution from a prominent young object featuring a break or a cutoff in the injection spectrum of e^\pm pairs.

In order to do so, we consider four different scenarios, deriving from the combination of two limit behaviours of the luminosity function (*i.e.* burst-like injection and constant-luminosity injection) with the two possibilities for the injection feature (*i.e.* exponential cutoff and break).

These are parametrized in the single-source term $Q(E, r, t)$ of the transport equation (3.6) (for a detailed discussion on the solutions here used, we refer again to Appendix A).

In each case, the properties of the young, dominant object are assessed by means of a Bayesian fit. We implement our theoretical knowledge of the problem by setting priors on the injection index, that we expect to be $\Gamma_{\text{inj}} \in [1, 2]$, and on the critical energy above which we expect the injection feature to come into play, $E_{\text{cut, break}} > 150 \text{ GeV}$. For the burst-like injection we consider the age and distance of the Monogem pulsar, while for the constant-luminosity we use age and distance of Geminga. This is accordance to what is shown and discussed in Appendix D, where all the high-energy nearby (within 1.3 kpc) sources are plotted in both injection scenarios, and the dominant contribution is assessed in both cases.

The resulting plots are shown in Figure 3 and the *Maximum-a-Posteriori* (MAP) parameters of the fits are listed in Tables 2 and 3.

We notice that each of the four combinations is compatible with the positron data. The corner plots shown in Appendix B outline a regular and well-behaved set of *posterior distribution functions* (PDF). Nonetheless, comparing the numerical values on the tables, relevant physical aspects have to be noticed:

- Even though we set a prior for the injection indices to be hard, data seem to favorite the very-hard end of the range: all the cases present $\Gamma_{\text{inj}} \lesssim 1.3$, with the softest being the burst-like injection with intrinsic cutoff.

³Interestingly, their model E1 — which is characterized by diffusion and loss parameters very close to those adopted in this work — predicts a positron fraction steadily growing with energy up to 100 GeV; above that energy, the fraction flattens reaching a maximum at about 300 GeV.

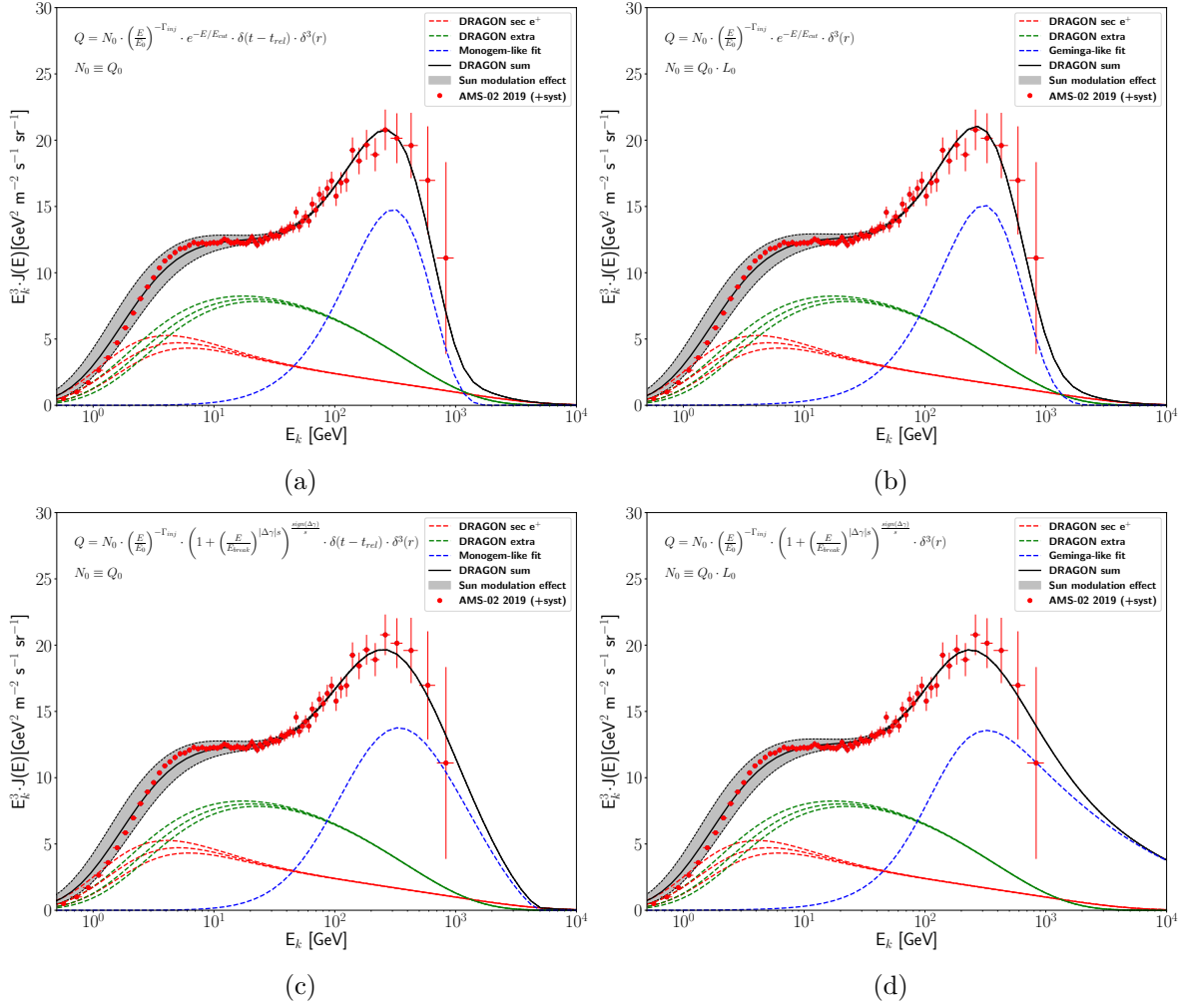


Figure 3: Bayesian fit to the positron flux within two classes of different injection scenarios, where intrinsic features are added. (a) Burst-like injection with cutoff, (b) constant-luminosity injection with cutoff, (c) burst-like injection with broken power-law, (d) constant-luminosity injection with a broken power-law.

	N_0	Γ_{inj}	E_{cut} [GeV]	E_{tot} [erg]	η^\pm
Burst	$2.4 \cdot 10^{48} [\text{GeV}]^{-1}$	1.31	270.78	$2 \cdot 5.39 \cdot 10^{46}$	—
L_0	$1.17 \cdot 10^{35} [\text{GeV} \cdot \text{s}]^{-1}$	1.07	200.43	$2 \cdot 2.02 \cdot 10^{45}$	$< 1.2 \cdot 10^{-2}$

Table 2: Our MAP values for the injection-parameters from e^\pm sources with an intrinsic cutoff, set to have a prior distribution with $E_{\text{cut}} > 150$ GeV. The total energy injected in the ISM in the form of leptons is indirectly computed from the fit-parameters: the factor 2 is multiplied because of the e^\pm symmetry. Only in the $L(t) \approx L_0$ limit case, which corresponds to a dominating magnetic-dipole emission, the conversion efficiency η^\pm is computed with respect to the nominal ATNF observed parameters: it is an upper bound because it is used the rate of energy-loss at the current time.

- For the burst-like solutions the injection features are found at energies higher ($E_{\text{cut,break}} > 270$ GeV) with respect to the constant-luminosity case ($E_{\text{cut,break}} \lesssim 200$ GeV): this ef-

	N_0	Γ_{inj}	$\Delta\gamma$	E_{break} [GeV]	s	E_{tot} [erg]	η^\pm
Burst	$1.08 \cdot 10^{48} [\text{GeV}]^{-1}$	1.02	-2.77	321.65	0.31	$2 \cdot 2.35 \cdot 10^{47}$	—
L_0	$1.11 \cdot 10^{35} [\text{GeV} \cdot \text{s}]^{-1}$	1.10	-1.74	158.02	1.11	$2 \cdot 3.35 \cdot 10^{47}$	$\lesssim 1$

Table 3: Our MAP values for the injection-parameters from e^\pm sources with an injection break, parametrized by the multiplying factor $\left(1 + \left(\frac{E}{E_{\text{break}}}\right)^{|\Delta\gamma| \cdot s}\right)^{\text{sign}(\Delta\gamma)/s}$, set to have a prior distribution with $E_{\text{break}} > 150$ GeV. The total energy injected in the ISM in the form of leptons is indirectly computed from the fit-parameters: the factor 2 is multiplied because of the e^\pm symmetry. Only in the $L(t) \approx L_0$ limit case, which corresponds to a dominating magnetic-dipole emission, the conversion efficiency η^\pm is computed with respect to the nominal ATNF observed parameters.

fect is due to the peculiar shape of the burst-like solution, which features a sharp cutoff that is required to match the drop-off of the data.

- The total amount of energy converted into e^\pm pairs is estimated by means of:

$$E_{\text{tot}} = \int_{E_{\text{min}}}^{E_{\text{max}}} dE \int_{t_{\text{rel}}}^{t_{\text{age}}} dt \int d^3\vec{r} E \cdot Q(E, \vec{r}, t), \quad (3.9)$$

where $E_{\text{min}} = 1$ GeV and $E_{\text{max}} = +\infty$: only in the cases of logarithmic divergences a cut at very high-energies ($E_{\text{cut}} = 100$ TeV) is set. Equation (3.9) gives values compatible with the order-of-magnitude energies that are thought to be injected by pulsars in the ISM. Besides, an efficiency is estimated with respect to the nominal ATNF parameters, for the constant-luminosity solutions only. As a matter of fact, this is because the ATNF Catalogue is assembled assuming magnetic-dipole emission, but then the nominal values give a ratio $t_{\text{ch}}/\tau_0 \ll 1$, resulting in the constant-luminosity limiting case. In particular, with a broken power-law, the efficiency is close to 1, but this can be due to an underestimation of the nominal total-energy injected by the pulsar into the ISM, as it is argued in Appendix D.

In conclusion, in this section we found that scenarios characterized by a prominent young pulsar that dominates the high-energy positron flux, and a large number of middle-aged and old pulsars — modeled as a continuous contribution to the flux — are compatible with current data, under different hypotheses on both the injection spectrum and the timescale of the luminosity decline. The best-fit values for the injection spectra are compatible with the physical mechanisms outlined at the beginning of the sections. However, different scenarios correspond to different estimates of the total energy budget and to a different hierarchy of the contributions from the nearby pulsars, as shown in Figure 8. Therefore, given the current data and the current knowledge on the physics of pulsar wind nebula emission, it is not possible to clearly identify which objects actually provide the most relevant contribution to the positron flux.

4 Local electron accelerators explain the high-energy electron data

This section is dedicated to the interpretation of the all-lepton spectrum. We adopt the best-fit CR transport scenario evaluated in Section 2 and the e^\pm (assumed charge symmetric) factories are included according to the positron-flux fit discussed in the previous section.

	t_{age} [yr]	d [pc]	$r_{\text{diff},1 \text{ TeV}}$ [pc]	$r_{\text{diff},10 \text{ TeV}}$ [pc]	$\frac{r_{\text{diff},1 \text{ TeV}}}{d}$	$\frac{r_{\text{diff},10 \text{ TeV}}}{d}$
Vela Jr	$2.5 \cdot 10^3$	214.2	$1.08 \cdot 10^2$	$1.82 \cdot 10^2$	0.51	0.85
Vela	$1.23 \cdot 10^4$	250.92	$2.69 \cdot 10^2$	$4.52 \cdot 10^2$	1.07	1.80
Cygnus L	$8 \cdot 10^3$	449.82	$2.17 \cdot 10^2$	$3.64 \cdot 10^2$	0.48	0.80
Simeis-147	$4 \cdot 10^4$	918	$4.85 \cdot 10^2$	$8.14 \cdot 10^2$	0.52	0.89
IC-443	$3 \cdot 10^4$	918	$4.20 \cdot 10^2$	$7.05 \cdot 10^2$	0.46	0.77

Table 4: The nominal ages and distances of the five closest observed SNRs are listed. The diffusive distances are also shown for particles of 1 TeV and 10 TeV, in order to have a clear look on the sources that can contribute to the multi-TeV lepton flux. For a comparison with the loss-properties, $r_{\text{loss},1 \text{ TeV}} \simeq 1.15 \cdot 10^3$ pc and $r_{\text{loss},10 \text{ TeV}} \simeq 6.13 \cdot 10^2$ pc. From the numbers, Vela seems the one that can contribute the most to the $e^+ + e^-$ flux.

Under these assumptions, we find that the high-energy lepton flux must be dominated by local, electron-only sources. We will show that the closest observed SNRs are not sufficient to describe the observed spectrum and an additional source with specific characteristics has to be invoked to reproduce in particular the ~ 1 TeV break recently measured by the space-born and ground-based experiments H.E.S.S., VERITAS, CALET and DAMPE. Although no information is provided on the nature of the object, we model it as a SNR, because these objects are expected to be the bulk of CRs observed at the Earth, mainly based on energetic arguments (see for instance [66]).

4.1 Contribution from the known objects

Multi-wavelength observations show the presence of five Supernova Remnants (SNRs) in the local region (within ~ 1 kpc) surrounding the Earth⁴ [67], identified with the names Vela Jr, Vela, Cygnus Loop, Simeis-147, IC-443.

We report in Table 4 the nominal ages and distances of these objects and the distances that particles with 1 TeV and 10 TeV can travel in the ISM via diffusive transport, as well as the ratios between the diffusive distance and the distance of the source. We outline that, given the values reported in that table, the contribution of Vela Jr — the youngest remnant in the set under consideration — should peak around ~ 100 TeV, where we do not have reliable data. As far as the others are concerned, Vela is expected to provide the most relevant contributions; the other ones are expected to be subdominant, since the diffusive distance is smaller than the nominal distance, but not negligible. Therefore, we choose to take into account all the remnants listed above with the only exception of Vela Jr.

In order to estimate the contributions from the sources mentioned above, we perform a Bayesian fit in which each SNR is modeled as a continuous source of e^- . It is possible to parametrize the problem with the same formalism we used for the pulsar decaying-luminosity injection, *i.e.* the luminosity-function can be written as:

$$L(t) = \frac{L_0}{\left(1 + \frac{t}{\tau_d}\right)^{\alpha_d}}, \quad (4.1)$$

⁴<http://www.physics.umanitoba.ca/snr/SNRcat>

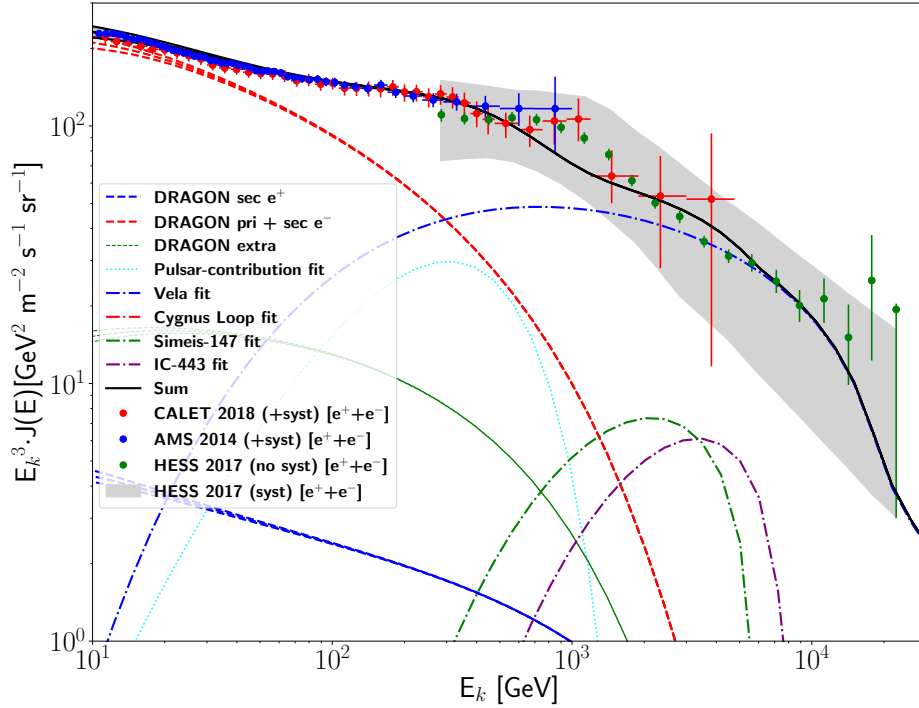


Figure 4: Bayesian fit of the $e^+ + e^-$ flux. The secondary and primary production and the extra-component, along with the fitted pulsar contribution, are considered as background, while the four SNRs have their parameters resulting from the fit. The sources are not able to reproduce the ~ 1 TeV observed break.

where now τ_d and α_d are specific for the release from a SNR and have nothing to do with pulsar injection mechanisms, and t is as usual the age of the source. The particle propagation is accounted for by solving the transport equation as described in Appendix A.

The parameters we vary in the fitting procedure are the flux normalization, the injection index, and the luminosity decline parameters (τ_d, α_d) of the sources. Based on the physical assumption that the acceleration mechanism is the *diffusive shock acceleration* (DSA) [15–18], a prior is set for the injection indices to be $\Gamma_{\text{inj}} \in [2, 3]$ [68, 69]. The parameters (τ_d, α_d) are allowed to vary, but are set as identical for each source: we verified that this approximation has a minimal impact on the final result, for values in the ranges $10^3 < \tau_d < 10^6$ yr and $1 < \alpha_d < 3$, due to the relatively large distance of the sources of our interest.

The results are shown in Figure 4, and the maximum a posteriori parameters listed in Table 5.

As expected, the main contribution comes from the Vela SNR, due to the interplay among the diffusive distance, the distance of the source and the energy-loss characteristic distance. Simeis-147 and IC-443 cannot give contribution to the $\mathcal{O}(10 \text{ TeV})$ flux, since their distance is larger than the loss distance at this energy, and indeed their peaks lie at energies smaller than $\sim 8 \text{ TeV}$. The contribution from Cygnus Loop is extremely suppressed and even not visible in the plot, because the source is younger than the others and its peak would appear at too-high energy to be compatible with the data. Finally, the energy budgets of the sources are compatible with the amount of energy that are expected by SNR events ($\sim 10^{51}$ erg), taking into account the conversion efficiency into leptons within the range

	N_0 [GeV · s] ⁻¹	Γ_{inj}	τ_d [yr]	α_d	E_{tot} [erg]
Vela	$1.31 \cdot 10^{41}$	2.84	$1.87 \cdot 10^3$	2.47	$9.52 \cdot 10^{48}$
Cygnus L	$6.11 \cdot 10^{39}$	2.95			$3.78 \cdot 10^{47}$
Simeis-147	$3.98 \cdot 10^{42}$	2.98			$2.59 \cdot 10^{50}$
IC-443	$1.03 \cdot 10^{41}$	2.93			$7.04 \cdot 10^{48}$

Table 5: The table reports the MAP parameters resulting from the bayesian fit. Also, the total energy injected by each source in the form of e^\pm is computed, based on the normalization.

	N_0 [GeV · s] ⁻¹	Γ_{inj}	τ_d [yr]	α_d	t_{age} [yr]	d [pc]	E_{tot} [erg]
1 hidden	$2.14 \cdot 10^{39}$	2.25	$1.13 \cdot 10^5$	2.40	$1.54 \cdot 10^5$	658.21	$2.45 \cdot 10^{49}$
4+1 hidden	$6.10 \cdot 10^{39}$	2.05	$4.97 \cdot 10^3$	2.45	$4.97 \cdot 10^5$	$1.19 \cdot 10^3$	$1.94 \cdot 10^{49}$

Table 6: The table reports the MAP parameters resulting from the bayesian fit to the all-lepton flux. The **1 hidden** scenario identifies the case where only an unknown object is considered, while **4+1 hidden** fits an unknown SNR on top of the observed SNRs. The total energy injected by each source in the form of e^\pm is also computed, based on the normalization.

$\eta^\pm \sim 10^{-4}, \dots, 10^{-1}$ [70], due to physical phenomena such as the particle escape at the shock front [71, 72].

The most relevant implication of this result is that the ~ 1 TeV spectral break cannot be reproduced with known sources. In fact, as noticed in [73], the propagated spectrum from a nearby SNR would peak at that energy for a source as old as $\sim 2 \cdot 10^5$, a much larger age compared to that of the sources considered here.

4.2 Characterization of a potential source reproducing the ~ 1 TeV break

A Bayesian fit of the data with the emission of all the known sources in the current catalogs shows that either a radical change in the propagation paradigm or an unknown source are needed. In particular, an old ($\sim 10^5$ yr) SNR seems to be necessary to reproduce correctly the ~ 1 TeV break, as first pointed out in [73].

In order to better characterize this potential source we perform a fit of the data in two different scenarios:

- 1) None of the listed known sources contribute to the flux,
- 2) All of them add their contributions to the flux.

The free parameters in both cases are the normalization, the injection index, the (τ_d, α_d) luminosity parameters, the age and distance of the source. We set a flat prior for the injection index in the range $\Gamma_{\text{inj}} \in [2, 3]$, since we assume DSA to be the acceleration mechanism at work. In the second case, we also assume a flat prior for the distance in the range $d < 1.2 \cdot 10^3$ pc, because we do not expect ~ 1 TeV leptons to come from more distant sources, given the energy loss mechanisms.

The outcome of this procedure is shown in 1) Figure 5a and 2) Figure 5b and the parameters summarized in Table 6.

As a result of this analysis, we find that a hidden old remnant of $\sim 10^5$ yr is actually needed to reproduce correctly the data, and the best-fit distance is expected to be in the range (600 – 1200) pc. This range of distances is different from the value quoted in [73], where a close source ($d = 100$ pc) is invoked to match the observed data. The discrepancy is mainly due to the propagation setup: we find that, in accordance with [73], such a close source would correctly reproduce the data only if a diffusion coefficient with a Kolmogorov-like rigidity scaling ($\delta = 0.33$) and a smaller normalization were assumed. We remark that our reference transport scenario with $\delta = 0.45$ is compatible with the MCMC analysis carried out in [45]. We also mention that a different interpretation for this feature based on an additional pulsar has been proposed [74].

Given the required age, such a remnant would most likely be in its final *radiative* phase and may be not clearly detectable. The SNR catalogue [67] reports a possible candidate that we find particularly interesting, the Monogem Ring, which is categorized as *uncertain SuperNova Remnant*. However, this source is too close ($d < 300$ pc) to the Earth and its propagated spectrum does not seem to be compatible with the high-energy ($E > 10$ TeV) all-lepton data, according to our propagation scenario, in particular due to our diffusion coefficient rigidity scaling ($\delta = 0.45$) and normalization.

5 Conclusions

In this paper we provided a comprehensive discussion about the origin of the most relevant features observed in the positron, electron and all-lepton data recently released by the AMS-02, CALET, and H.E.S.S. Collaborations.

We first identified a CR transport scenario that provides a very good description of accurate B/C data published by AMS-02, and the proton, He, C and O data measured by AMS-02 and Voyager.

With this propagation setup at hand, we considered the positron data, which show a remarkable excess with respect to the secondary flux expected from the conventional proton-proton spallation process, and studied the expected contribution from individual pulsar wind nebulae (PWNe). Starting from a careful study of the analytical solution of the diffusion-loss equation from individual sources, we characterized the contribution due to a large number of old PWNe as a large scale extra-component which is often neglected in the related literature. Then we focused on the prominent peak and drop-off in the positron spectrum recently found by AMS-02 around 300 GeV. After pointing out as that feature is not compatible with alternative scenarios in which the largest part of the positron population is originated by CR nuclei scattering onto the ISM gas, we described it in terms of the emission from a young PWN under different conditions. We found that a hard acceleration spectrum and a spectral break or a cutoff at few hundred GeV are required to match the data, which is consistent with recent theoretical modeling of the typical acceleration mechanisms at the termination shock of PWNe.

Finally, we turned our attention to the all-lepton spectrum and tried to reproduce its shape accounting for the contribution of known and possibly hidden SNRs.

We noticed that the contribution of local SNRs takes over the softer large-scale component at $\simeq 40$ GeV. We found however that the contribution of known nearby SNRs cannot reproduce the TeV feature recently identified by the H.E.S.S. Collaboration. Then, building on previous results from [73], we found that if a relatively near, old remnant is included in the calculation, with declining luminosity and with age $\sim 10^5$ yr and distance in the 600 – 1200

pc range, the data are nicely reproduced within the propagation setup described in the first part, consistently with all the hadronic and leptonic channels under consideration.

Acknowledgments

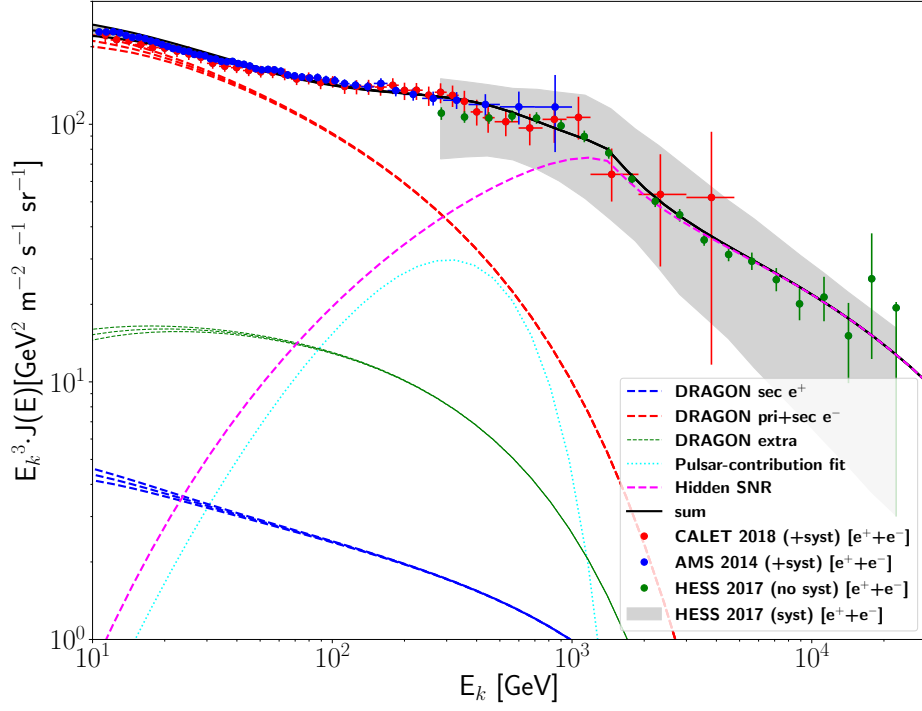
We are grateful to E. Amato, C. Evoli, S. Gabici, and S. Recchia for very inspiring discussions.

The work of DG has received financial support through the Postdoctoral Junior Leader Fellowship Programme from la Caixa Banking Foundation (grant n. LCF/BQ/LI18/11630014). DG was also supported by the Spanish Agencia Estatal de Investigación through the grants PGC2018-095161-B-I00, IFT Centro de Excelencia Severo Ochoa SEV-2016-0597, and Red Consolider MultiDark FPA2017-90566-REDC.

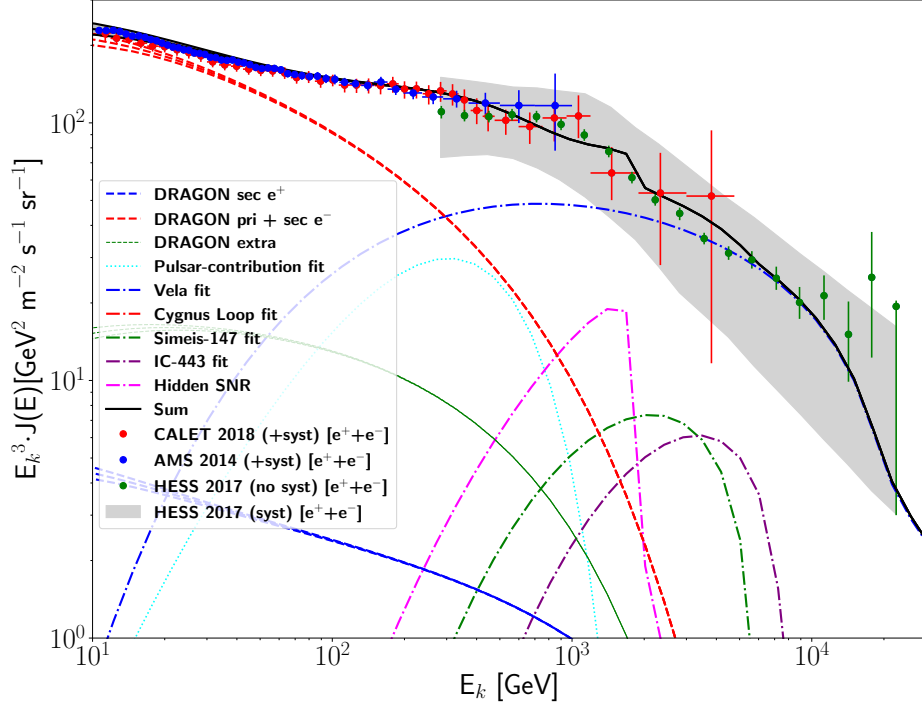
OF warmly thanks the Instituto de Física Teórica UAM-CSIC in Madrid, and in particular the DAMASCO group, for hosting him during the period January - June 2019 and La Caixa Banking Foundation (grant n. LCF/BQ/LI18/11630014) for partial financial support.

D. Grasso was supported by the grant ASI/INAF No. 2017-14-H.O.

We acknowledge the use of the IFT Hydra cluster for the development of part of this work.



(a)



(b)

Figure 5: Bayesian fits of the $e^+ + e^-$ flux: the secondary and primary production, the extra-component and the fitted pulsar contribution, are considered as background. An additional hidden SNR with free parameters $N_0, \Gamma_{\text{inj}}, \alpha_d, \tau_d, t_{\text{age}}, r_{\text{dist}}$ is fitted when: (a) no known SNR is taken into account, (b) contributions from all the observed SNRs are also considered.

A Single-source solution to the transport equation

In this appendix we summarize the results of the general treatment made by [25, 54], which contains the analytical solutions to the transport equation in different injection scenarios.

Comparing the timescales for diffusion ($\tau_{\text{diff}} = \frac{H^2}{2D(E)}$) and advection ($\tau_{\text{adv}} = \frac{H}{v_A}$), with standard average Interstellar Medium (ISM) conditions (which lead to $v_A \sim 10$ km/s), a Halo size of $H = 4$ kpc and a diffusion coefficient resulting from our analysis in the text ($D(E) = 1.98 \cdot 10^{24} \left(\frac{E}{1 \text{ GeV}}\right)^{0.45} \text{ m}^2/\text{s}$) we see that advection is a significant process below ~ 100 MeV. As we are interested in a high-energy regime (above ~ 1 GeV), we can neglect the advection term and write the transport equation in polar coordinates as follows:

$$\frac{\partial f(E, t, r)}{\partial t} = \frac{D(E)}{r^2} \frac{\partial}{\partial r} r^2 \frac{\partial f}{\partial r} + \frac{\partial}{\partial E} (b(E)f) + Q, \quad (\text{A.1})$$

where $b(E)$ is the rate of energy-loss and $Q(E, t, \vec{r})$ the source term. In the high-energy regime, where Inverse Compton and Synchrotron losses dominate, the energy-loss is given by $b(E) = -b_0 E^2$, with $b_0 = 1.4 \cdot 10^{-16} \text{ GeV}^{-1} \cdot \text{s}^{-1}$, according to Equation (3.7).

Under the assumption that the emitting source is point-like, the Green-function approach to solve the equation gives the general solution [25]:

$$f(r, t, E) = \frac{Q(E_t)b(E_t)}{\pi^{3/2}b(E)r_{\text{diff}}^3} \cdot e^{-\frac{r^2}{r_{\text{diff}}^2}}, \quad (\text{A.2})$$

where we drop the dependence of the source term Q on t and r for simplicity. E_t refers to the energy at a time $(t - t_{\text{rel}})$ ago, that, given the currently-measured energy E and the rate of energy-loss $b(E) = -b_0 E^2$, is $E_t = \frac{E}{1 - b_0(t - t_{\text{rel}})E}$. Therefore, the solution in Equation (A.2) becomes:

$$f(r, t, E) = \frac{Q(E_t)}{\pi^{3/2}r_{\text{diff}}^3} \cdot \frac{1}{[1 - b_0(t - t_{\text{rel}})E]^2} \cdot e^{-\frac{r^2}{r_{\text{diff}}^2}}, \quad (\text{A.3})$$

where $r_{\text{diff}}^2(E_t, E) \equiv -4 \int_{E_t}^E \frac{D(E')}{b(E')} dE'$ is the diffusive distance travelled by a particle losing its energy from E_t to E . This solution is still general, in that it does not contain any information about the injection term, that in general can be written $Q(t, r, E) = S(E)L(t)\delta(r)$, where we assume a power-law spectrum with index Γ_{inj} , $S(E) = S_0 \left(\frac{E}{E_0}\right)^{\Gamma_{\text{inj}}}$.

Decaying-luminosity injection. When no further information is provided on the luminosity timescale, the decaying-luminosity function is in the general form $L(t) = \frac{L_0}{\left(1 + \frac{t}{\tau_d}\right)^{\alpha_d}}$, with α_d and τ_d parameters characteristic of the emission mechanism. Integrating over time the expression (A.3), we obtain:

$$f(r, t_{\text{age}}, E) = \int_{t_{\text{rel}}}^{t_{\text{age}}} dt' \frac{S(E_{t'})L(t')}{\pi^{3/2}r_{\text{diff}}^3(E, E_{t'})} \cdot \frac{1}{[1 - b_0(t_{\text{age}} - t')E]^2} \cdot e^{-\frac{r^2}{r_{\text{diff}}^2}}, \quad (\text{A.4})$$

where t_{rel} is the release time of the particles.

Equation (A.4) is the most general form of the solution and it can be notice that, as the integration over time is not performed yet, any injection feature can still be easily implemented in the expression of $S(E)$. In particular, in this work we will use source features such as an exponential cutoff or a break in the power-law:

$$\begin{aligned}
- S(E) &= S_0 \left(\frac{E}{E_0} \right)^{\Gamma_{\text{inj}}} \cdot e^{-\frac{E}{E_{\text{cut}}}} \\
- S(E) &= S_0 \left(\frac{E}{E_0} \right)^{\Gamma_{\text{inj}}} \cdot \left(1 + \left(\frac{E}{E_{\text{break}}} \right)^{|\Delta\Gamma_{\text{inj}}|s} \right)^{\text{sign}(\Delta\Gamma_{\text{inj}})/s},
\end{aligned}$$

where $\Delta\Gamma_{\text{inj}}$ is the change in the injection index and s a parameter that rules the sharpness of the change in the slope. It can be easily seen that in the two limits $E \ll E_{\text{break}}$ and $E \gg E_{\text{break}}$ we find the two different power-laws.

Constant-luminosity injection. This is a physical scenario that corresponds to the limiting case of (A.4) where the luminosity timescale τ_0 is much larger than the age of the source. Based on this, the luminosity function can be approximated by $L(t) \rightarrow L_0 dt$.

Beside, if the injection function $S(E)$ does not have any dependence on time, the integral is easily performed and the solution takes the form:

$$f(r, t_{\text{age}}, E) = \frac{L_0 S(E)}{4\pi D(E)r} \cdot \text{erfc} \left(\frac{r}{\sqrt{4D(E)(t_{\text{age}} - t_{\text{rel}})}} \right), \quad (\text{A.5})$$

with $\text{erfc}(x) = \frac{2}{\sqrt{\pi}} \int_x^\infty e^{-t^2} dt$ the complementary error-function.

Burst-like injection. This scenario corresponds to the opposite limit with respect to the previous one, namely the case where τ_0 is much smaller than the age of the source. The luminosity function is therefore $L(t) \rightarrow L_0 \delta(t - t_{\text{rel}}) dt$, and the solution (A.4) basically takes the form of the integrand function:

$$f(r, t_{\text{age}}, E) = \frac{S(E_{t_{\text{age}}})}{\pi^{3/2} r_{\text{diff}}^3(E, E_{t_{\text{age}}})} \cdot \frac{1}{[1 - b_0(t_{\text{age}} - t_{\text{rel}})E]^2} \cdot e^{-\frac{r^2}{r_{\text{diff}}^2}}. \quad (\text{A.6})$$

It is worth mentioning that any injection features such as the ones discussed before (*i.e.* cutoff and break) can be implemented at this step without worrying about the time integration, due to the presence of the delta function.

The decaying-luminosity and burst-like solutions are valid as long as the condition $1 - b_0(t_{\text{age}} - t_{\text{rel}})E \neq 0$ holds, that can also be written as $E \neq \frac{1}{b_0(t_{\text{age}} - t_{\text{rel}})}$. However, this expression represents the maximum energy that a particle can have after a time $(t_{\text{age}} - t_{\text{rel}})$ spent in the Galaxy. Therefore, the condition becomes immediately $E < \frac{1}{b_0(t_{\text{age}} - t_{\text{rel}})}$. This condition translates into a sharp cutoff in the spectrum for the burst injection and for a peak in the case of decaying luminosity. After this peak, the release time t_{rel} grows and the maximum energy becomes larger, even though the normalization decreases due to the smaller luminosity. This behaviour does not occur for the constant-luminosity scenario, where emission lasts constantly up the current time t_{age} , represented indeed by the simpler mathematical condition $t_{\text{age}} - t_{\text{rel}} > 0$.

B Posterior distribution functions for the fit to the positron flux

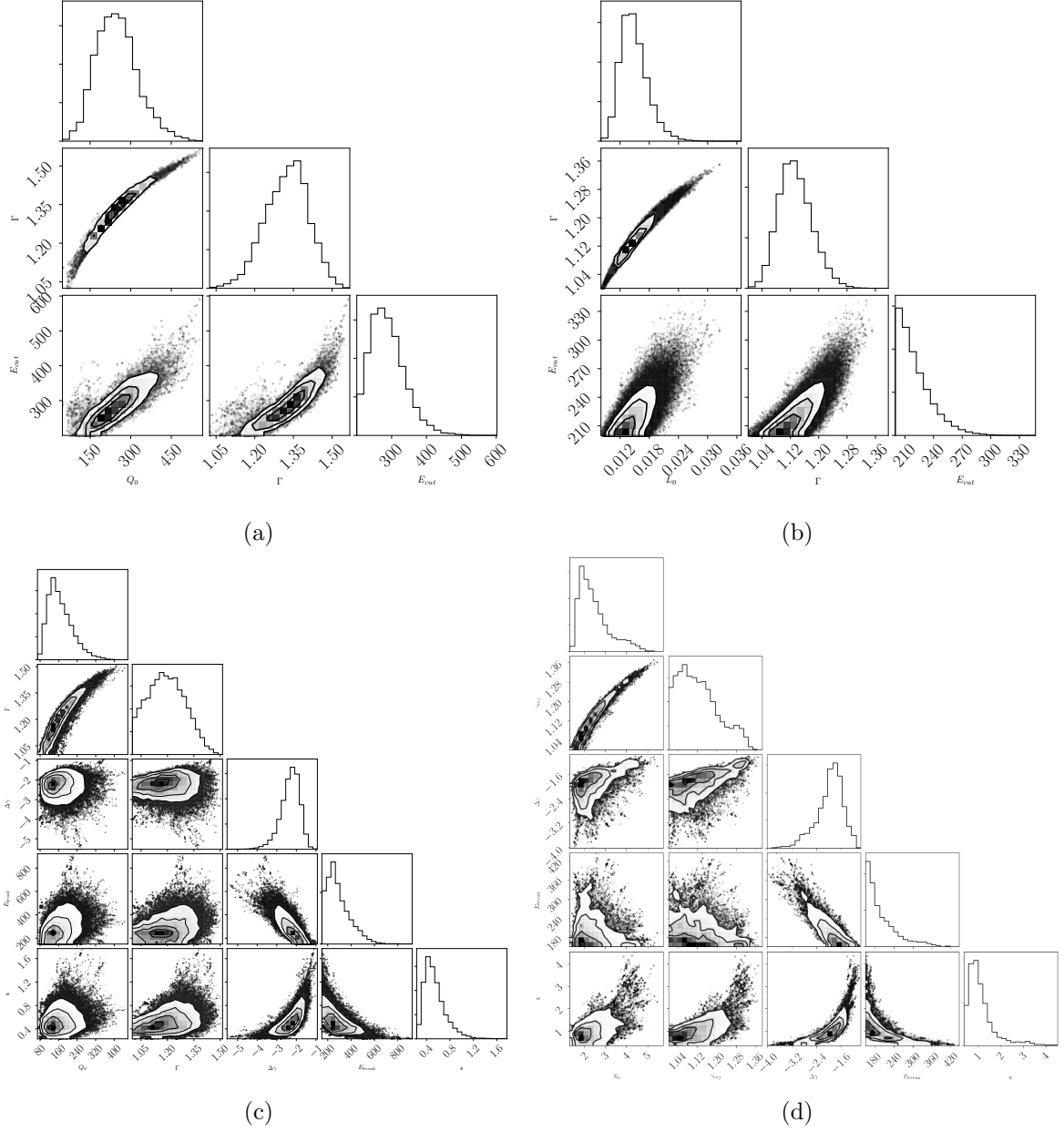


Figure 6: Posterior distribution functions of the bayesian fit to the positron flux, corresponding to the four different scenarios discussed in the text: (a) burst-like injection with exponential cutoff, (b) constant-luminosity injection with exponential cutoff, (c) burst-like injection with broken power-law, (d) constant-luminosity injection with broken power-law.

C Estimation of the release time from PWNe

Since the release of the PAMELA data on the positron fraction, several phenomenological scenarios invoked a relevant delay between pulsar formation and the release of the elec-

tron+positron pairs in the ISM (see for instance [75]). The physical picture behind this time delay, extensively discussed for example in [60], is the following. A typical pulsar forms in a core collapse supernova event with a natal kick velocity of $\simeq 400$ km/s or larger; this relevant proper motion drives the compact object far from the place of its formation, across the supernova remnant and then across the shocked ejected material. After the escape from the remnant, as a consequence of the impact of the relativistic PWN wind onto the ISM, a bow shock forms. Such structure can hardly confine the electron+positron pairs accelerated within the PWN: the particles can hence escape from the PWN and contribute to the diffuse sea of cosmic radiation.

In this work, guided by this physical picture, we estimate the release time by computing the time needed by a pulsar with a typical kick velocity to escape a typical SN Ia remnant. The time evolution of the SNR shock radius is computed following the prescriptions summarized in [76]. In particular, the ejecta-dominated phase is described by the self-similar solutions provided by [77], and the subsequent Sedov phase is modeled adopting the thin-shell approximation [78], based on the assumption that the mass is mostly concentrated within a shell of negligible thickness at the forward shock. Given these assumptions on the SNRs, and within a wide range of pulsar kicks, spanning from 100 to 1000 km/s, we obtain release times in the interval $[10^4 - 5 \cdot 10^5]$ yr. For the purpose of this work, we consider an intermediate reference value $t_{\text{rel}} = 6.4 \cdot 10^4$ yr, that corresponds to a pulsar with kick $v_{\text{pulsar}} = 400$ km/s.

D Notes on the pulsars from ATNF Catalogue

The position of the peak in the positron flux data (~ 250 GeV) requires sources that are as old as $\sim 10^6$ yr, based on $E_{\text{peak}} = 1/(b_0 \cdot (t_{\text{ch}} - t_{\text{rel}}))$. A particle diffusing in the Galaxy for this time interval is coming from a distance $\sqrt{4 \cdot D(E_{\text{peak}}) \cdot (t_{\text{ch}} - t_{\text{rel}})} \simeq 1.3$ kpc.

In Figure 7 we report all the pulsars listed in the ATNF Catalogue that are found within this distance and younger than $2 \cdot 10^8$ yr. We make them inject leptons with a hard spectrum ($\Gamma_{\text{inj}} = 1.5$) up to an energy $E_{\text{cut}} = 300$ GeV, where an exponential cutoff $e^{-\frac{E}{E_{\text{cut}}}}$ is implemented. This is according to [20], where it is argued that pulsar emission requires a break in the observed spectrum due to a change in the accelerating site around the compact object: leptons up to 200 – 400 GeV are accelerated within the nebula by mechanisms that are not fully understood (*e.g.* magnetic reconnection), with a hard injection $\Gamma_{\text{inj}} < 2$, while more energetic leptons are accelerated at the termination shock, thus with a softer spectrum $\Gamma_{\text{inj}} > 2$ characteristic of the DSA acceleration mechanism. While it is not clear whether the second population can be considered subdominant, thus justifying a cutoff instead of a break, this does not affect much the energy budget injected by the source, therefore it is not crucial specifying it for a proof of concept. After injection, we make them propagate through the Galaxy via the transport-equation (A.1).

For the release time of the leptons, we consider the value $t_{\text{rel}} = 6.4 \cdot 10^4$ yr, corresponding to a pulsar with birth speed $v_{\text{pulsar}} = 400$ km/s, as described in Appendix C. We checked the extreme values discussed there and verified that the results are qualitatively equivalent, although the contributing sources change, because sources younger than the release-time could not have released particles yet.

With this emission paradigm, we plot all the sources that in the figure are marked as *high-energy pulsars*. This denomination is due to the emission frequency, but we consider them because, as shown in the figure, they uniformly span the scatter plot and thus constitute a good sample. The result is shown in Figure 8, where the constant-luminosity (8a) and the

burst-like (8b) solutions to (A.1) are compared: only the constant luminosity injection can reproduce the positron data. This is due to the total amount of injected energy, that we estimated trivially as $E_{\text{tot}} = \dot{E}_{\text{loss}} \cdot t_{\text{ch}}$. As it can be easily understood, this is a lower bound, since it is based on the current measurements of the \dot{P} for \dot{E}_{loss} . Since the energy-loss is related to the slowing rotation of the pulsar, the rate of loss at the beginning of its life was larger than what it is now. We can do an attempt to improve the estimation for E_{tot} by implementing the magnetic dipole (MD) radiation model, as follows:

$$E_{\text{tot}} = \int_{t_{\text{rel}}}^{t_{\text{age}}} \dot{E}_{\text{MD}} dt, \quad (\text{D.1})$$

where $\dot{E}_{\text{MD}} = -\frac{B^2 R^6 \Omega^4}{6c^3}$, $\Omega(t) = \frac{\Omega_0}{\sqrt{1 + \frac{t_{\text{age}}}{\tau_{0,MD}}}}$.

Carrying out the integral, we obtain:

$$E_{\text{tot}} = \tau_{0,MD} \frac{B^2 R^6 \Omega_0^4}{6c^3} \cdot \left(\frac{1}{1 + \frac{t_{\text{rel}}}{\tau_{0,MD}}} - \frac{1}{1 + \frac{t_{\text{age}}}{\tau_{0,MD}}} \right). \quad (\text{D.2})$$

With the ATNF parameters, we actually find that the total amount of energy injected by mean of magnetic dipole emission is smaller than the lower bound roughly calculated. This gives us a hint that the emission mechanism requires some modification.

Regardless of the model we assume for pulsar injection, there are two model-independent aspects that we can observe:

1. There is a very different conversion efficiency: in fact, for given age t_{ch} and loss rate \dot{E}_{loss} , if a source is continuously emitting, then the total amount of energy injected in the ISM is much larger than in the burst-like case. Therefore to match with the observed leptons only a much smaller fraction of this energy could have been converted into leptons, as already mentioned in [60].
2. Among the dominant sources, the hierarchy is inverted between Monogem and Geminga: this is also as expected if one considers the interplay among the different nominal parameters of the two pulsars. As a matter of fact, for the case of a burst-like source, all the energy is injected instantaneously in the ISM, therefore the younger source dominates over the older one, because particles have had less time to loose energy, despite the difference they have in the total injected-energy computed as $E_{\text{tot}} = \dot{E}_{\text{loss}} \cdot t_{\text{ch}}$. On the other hand, for the constant-luminosity case, the sources are still emitting, therefore the discriminating parameter here is E_{tot} .

As a final remark, we see that in both scenarios, there is one source that dominates over the others by a factor of ~ 2 and this is why we parametrized the fits in Section 3.4 with one dominant source.

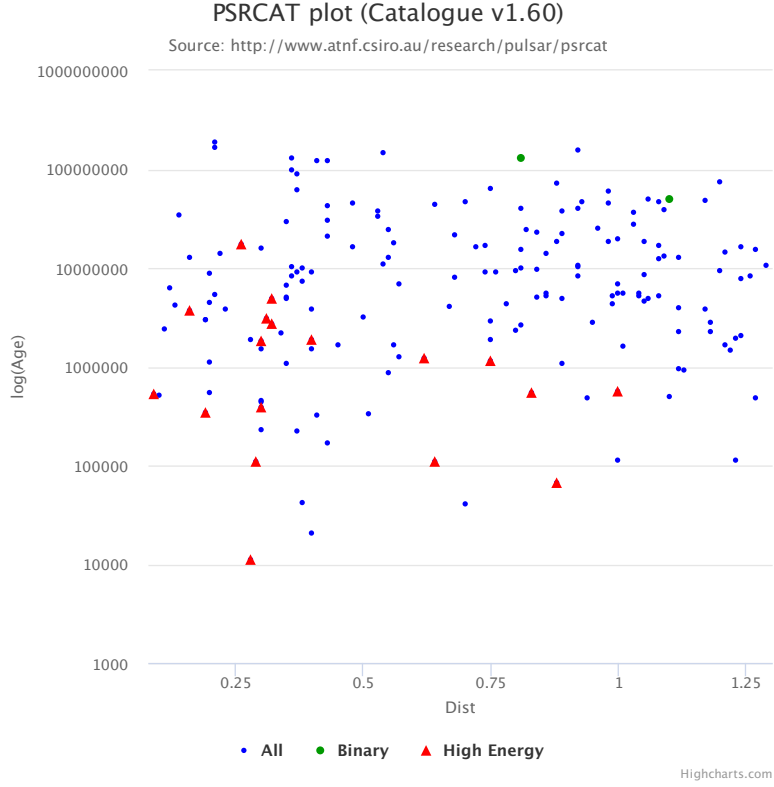


Figure 7: The figure is a $(d, \log_{10}(t_{\text{age}}))$ scatter plot of all the pulsars that ATNF Catalogue reports within 1.3 kpc and younger than $2 \cdot 10^8$ yr. Marked with red triangles there are high-energy pulsars, that have an emission at frequency higher than infrared. As they are distributed quite uniformly, we will consider them as a good sample.

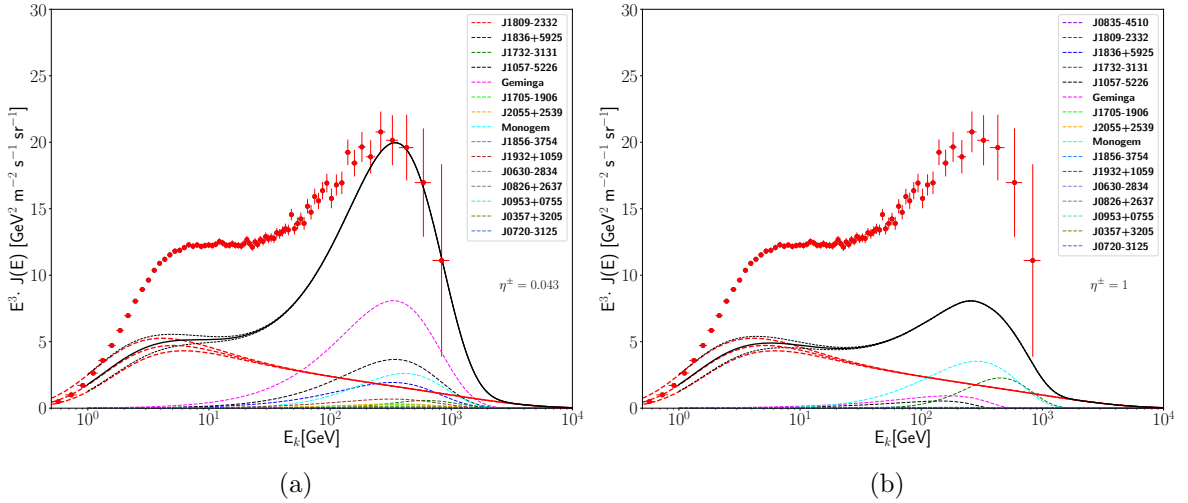


Figure 8: We plot here all the high-energy pulsars within 1.3 kpc and younger than $2 \cdot 10^8$ yr found in Figure 7, according to the nominal parameters of the ATNF Catalogue. (a) Sources are propagated from a constant luminosity injection, the high-energy data are reproduced with a conversion efficiency of $\eta^\pm = 0.043$. (b) Sources are propagated from a burst-like injection, the high-energy data cannot be matched, due to the insufficient nominal injected energy. Notice the inverted hierarchy of the dominant sources.

References

- [1] C. S. Shen. Pulsars and Very High-Energy Cosmic-Ray Electrons. *ApJL*, 162:L181, December 1970.
- [2] F. A. Aharonian, A. M. Atoyan, and H. J. Voelk. High energy electrons and positrons in cosmic rays as an indicator of the existence of a nearby cosmic tevatron. *A&A*, 294:L41–L44, February 1995.
- [3] T. Kobayashi, Y. Komori, K. Yoshida, and J. Nishimura. The Most Likely Sources of High-Energy Cosmic-Ray Electrons in Supernova Remnants. *ApJ*, 601:340–351, January 2004.
- [4] M. Aguilar et al. Towards Understanding the Origin of Cosmic-Ray Electrons. *Physical Review Letters*, 122(10):101101, March 2019.
- [5] F. Aharonian, A. G. Akhperjanian, G. Anton, U. Barres de Almeida, A. R. Bazer-Bachi, Y. Becherini, B. Behera, K. Bernlöhr, A. Bochow, and C. Boisson. Probing the ATIC peak in the cosmic-ray electron spectrum with H.E.S.S. *A&A*, 508(2):561–564, Dec 2009.
- [6] D. Kerszberg (for the H.E.S.S. Collaboration). The cosmic-ray electron spectrum measured with h.e.s.s. *International Cosmic Ray Conference, [CRI215] (2017)*.
- [7] G. Ambrosi et al. Direct detection of a break in the teraelectronvolt cosmic-ray spectrum of electrons and positrons. *Nature*, 552:63–66, 2017.
- [8] O. Adriani et al. Extended Measurement of the Cosmic-Ray Electron and Positron Spectrum from 11 GeV to 4.8 TeV with the Calorimetric Electron Telescope on the International Space Station. *Phys. Rev. Lett.*, 120(26):261102, 2018.
- [9] O. Adriani, G. C. Barbarino, G. A. Bazilevskaya, R. Bellotti, M. Boezio, E. A. Bogomolov, L. Bonechi, M. Bongi, V. Bonvicini, and S. Bottai. An anomalous positron abundance in cosmic rays with energies 1.5-100GeV. *Nature*, 458(7238):607–609, Apr 2009.
- [10] M. Aguilar et al. First Result from the Alpha Magnetic Spectrometer on the International Space Station: Precision Measurement of the Positron Fraction in Primary Cosmic Rays of 0.5–350 GeV. *Phys. Rev. Lett.*, 110:141102, 2013.
- [11] O. Adriani et al. Cosmic-Ray Positron Energy Spectrum Measured by PAMELA. *Physical Review Letters*, 111(8):081102, August 2013.
- [12] M. Aguilar et al. Electron and Positron Fluxes in Primary Cosmic Rays Measured with the Alpha Magnetic Spectrometer on the International Space Station. *Phys. Rev. Lett.*, 113:121102, 2014.
- [13] M. Aguilar et al. Towards Understanding the Origin of Cosmic-Ray Positrons. *Phys. Rev. Lett.*, 122(4):041102, 2019.
- [14] Paolo Lipari. Spectral shapes of the fluxes of electrons and positrons and the average residence time of cosmic rays in the Galaxy. *Phys. Rev.*, D99(4):043005, 2019.
- [15] R. D. Blandford and J. P. Ostriker. Particle acceleration by astrophysical shocks. *ApJL*, 221:L29–L32, April 1978.
- [16] A. R. Bell. The acceleration of cosmic rays in shock fronts. I. *MNRAS*, 182:147–156, January 1978.
- [17] W. I. Axford, E. Leer, and G. Skadron. The acceleration of cosmic rays by shock waves. *International Cosmic Ray Conference*, 11:132–137, 1977.
- [18] G. F. Krymskii. A regular mechanism for the acceleration of charged particles on the front of a shock wave. *Soviet Physics Doklady*, 22:327, June 1977.
- [19] P. D. Serpico. Possible causes of a rise with energy of the cosmic ray positron fraction. *Phys. Rev. D*, 79(2):021302, January 2009.

- [20] Elena Amato. The theory of pulsar wind nebulae. *Int. J. Mod. Phys. Conf. Ser.*, 28:1460160, 2014.
- [21] A. U. Abeysekara, A. Albert, R. Alfaro, C. Alvarez, J. D. Álvarez, R. Arceo, J. C. Arteaga-Velázquez, D. Avila Rojas, H. A. Ayala Solares, and A. S. Barber. Extended gamma-ray sources around pulsars constrain the origin of the positron flux at Earth. *Science*, 358(6365):911–914, Nov 2017.
- [22] Mattia Di Mauro, Silvia Manconi, and Fiorenza Donato. Detection of a γ -ray halo around Geminga with the Fermi-LAT and implications for the positron flux. *arXiv e-prints*, page arXiv:1903.05647, Mar 2019.
- [23] Dan Hooper, Ilias Cholis, Tim Linden, and Ke Fang. HAWC observations strongly favor pulsar interpretations of the cosmic-ray positron excess. *Phys. Rev. D*, 96(10):103013, Nov 2017.
- [24] V. L. Ginzburg and S. I. Syrovatskii. *The Origin of Cosmic Rays*. 1964.
- [25] V. S. Berezhinsky, S. V. Bulanov, V. A. Dogiel, and V. S. Ptuskin. *Astrophysics of cosmic rays*. 1990.
- [26] Carmelo Evoli, Daniele Gaggero, Dario Grasso, and Luca Maccione. Cosmic-Ray Nuclei, Antiprotons and Gamma-rays in the Galaxy: a New Diffusion Model. *JCAP*, 0810:018, 2008.
- [27] C. Evoli, D. Gaggero, A. Vittino, G. Di Bernardo, M. Di Mauro, A. Ligorini, P. Ullio, and D. Grasso. Cosmic-ray propagation with DRAGON2: I. numerical solver and astrophysical ingredients. *JCAP*, 2:015, February 2017.
- [28] Katia M. Ferriere. The interstellar environment of our galaxy. *Rev. Mod. Phys.*, 73:1031–1066, 2001.
- [29] Luke O’C Drury and Andrew W. Strong. Cosmic-ray diffusive reacceleration: a critical look. *PoS, ICRC2015*:483, 2016.
- [30] M. A. Gordon and W. B. Burton. Carbon monoxide in the Galaxy. I - The radial distribution of CO, H₂, and nucleons. *ApJ*, 208:346–353, September 1976.
- [31] L. Bronfman, R. S. Cohen, H. Alvarez, J. May, and P. Thaddeus. A CO survey of the southern Milky Way - The mean radial distribution of molecular clouds within the solar circle. *ApJ*, 324:248–266, January 1988.
- [32] A. W. Strong and G. Youssefi. Propagation Models For Cr Nucleons And Electrons And Predictions Of The Galactic Gamma-ray Spectrum. *International Cosmic Ray Conference*, 3:48, 1995.
- [33] A. W. Strong and I. V. Moskalenko. Propagation of cosmic-ray nucleons in the galaxy. *Astrophys. J.*, 509:212–228, 1998.
- [34] I. V. Moskalenko and A. W. Strong. Production and propagation of cosmic ray positrons and electrons. *Astrophys. J.*, 493:694–707, 1998.
- [35] M. S. Pshirkov, P. G. Tinyakov, P. P. Kronberg, and K. J. Newton-McGee. Deriving global structure of the Galactic Magnetic Field from Faraday Rotation Measures of extragalactic sources. *Astrophys. J.*, 738:192, 2011.
- [36] Carmelo Evoli, Daniele Gaggero, Andrea Vittino, Mattia Di Mauro, Dario Grasso, and Mario Nicola Mazziotta. Cosmic-ray propagation with DRAGON2: II. Nuclear interactions with the interstellar gas. *JCAP*, 1807(07):006, 2018.
- [37] W. R. Binns, T. L. Garrard, P. S. Gibner, M. H. Israel, M. P. Kertzman, J. Klarman, B. J. Newport, E. C. Stone, and C. J. Waddington. Abundances of ultraheavy elements in the cosmic radiation - Results from HEAO 3. *ApJ*, 346:997–1009, November 1989.

- [38] M. Aguilar et al. Precision measurement of the proton flux in primary cosmic rays from rigidity 1 gv to 1.8 tv with the alpha magnetic spectrometer on the international space station. *Phys. Rev. Lett.*, 114:171103, Apr 2015.
- [39] M. Aguilar et al. Observation of the identical rigidity dependence of he, c, and o cosmic rays at high rigidities by the alpha magnetic spectrometer on the international space station. *Phys. Rev. Lett.*, 119:251101, Dec 2017.
- [40] A. C. Cummings, E. C. Stone, B. C. Heikkila, N. Lal, W. R. Webber, G. Jóhannesson, I. V. Moskalenko, E. Orlando, and T. A. Porter. GALACTIC COSMIC RAYS IN THE LOCAL INTERSTELLAR MEDIUM:VOYAGER 1 observations AND MODEL RESULTS. *The Astrophysical Journal*, 831(1):18, oct 2016.
- [41] M. Aguilar et al. Precision measurement of the boron to carbon flux ratio in cosmic rays from 1.9 gv to 2.6 tv with the alpha magnetic spectrometer on the international space station. *Phys. Rev. Lett.*, 117:231102, Nov 2016.
- [42] I. G. Usoskin, K. Alanko-Huotari, G. A. Kovaltsov, and K. Mursula. Heliospheric modulation of cosmic rays: Monthly reconstruction for 1951-2004. *Journal of Geophysical Research (Space Physics)*, 110:A12108, December 2005.
- [43] I. G. Usoskin, G. A. Bazilevskaya, and G. A. Kovaltsov. Solar modulation parameter for cosmic rays since 1936 reconstructed from ground-based neutron monitors and ionization chambers. *Journal of Geophysical Research (Space Physics)*, 116:A02104, February 2011.
- [44] Giuseppe Di Bernardo, Carmelo Evoli, Daniele Gaggero, Dario Grasso, and Luca Maccione. Unified interpretation of cosmic-ray nuclei and antiproton recent measurements. *Astropart. Phys.*, 34:274–283, 2010.
- [45] Qiang Yuan, Su-Jie Lin, Kun Fang, and Xiao-Jun Bi. Propagation of cosmic rays in the AMS-02 era. *Phys. Rev.*, D95(8):083007, 2017.
- [46] Y. Genolini et al. Cosmic-ray transport from AMS-02 B/C data: benchmark models and interpretation. 2019.
- [47] Rebecca Diesing and Damiano Caprioli. On the Spectrum of Electrons Accelerated in Supernova Remnants. 2019.
- [48] Daniele Gaggero, Luca Maccione, Giuseppe Di Bernardo, Carmelo Evoli, and Dario Grasso. Three-Dimensional Model of Cosmic-Ray Lepton Propagation Reproduces Data from the Alpha Magnetic Spectrometer on the International Space Station. *Phys. Rev. Lett.*, 111:021102, 2013.
- [49] S. V. Bulanov and V. A. Dogel. The Influence of the Energy Dependence of the Diffusion Coefficient on the Spectrum of the Electron Component of Cosmic Rays and the Radio Background Radiation of the Galaxy. *Ap&SS*, 29(2):305–318, Aug 1974.
- [50] Oscar Adriani et al. An anomalous positron abundance in cosmic rays with energies 1.5-100 gev. *Nature*, 458:607–609, 2009.
- [51] Paolo Lipari. Interpretation of the cosmic ray positron and antiproton fluxes. *Phys. Rev. D*, 95(6):063009, Mar 2017.
- [52] Daniele Gaggero and Mauro Valli. Impact of cosmic-ray physics on dark matter indirect searches. *Adv. High Energy Phys.*, 2018:3010514, 2018.
- [53] A. K. Harding and R. Ramaty. The Pulsar Contribution to Galactic Cosmic Ray Positrons. *International Cosmic Ray Conference*, 2:92, 1987.
- [54] A. M. Atoyan, F. A. Aharonian, and H. J. Völk. Electrons and positrons in the galactic cosmic rays. *Phys. Rev. D*, 52:3265–3275, September 1995.
- [55] D. R. Lorimer and M. Kramer. *Handbook of Pulsar Astronomy*. December 2004.

- [56] O. Hamil, J. R. Stone, M. Urbanec, and G. Urbancová. Braking index of isolated pulsars. *Phys. Rev. D*, 91(6):063007, March 2015.
- [57] R. N. Manchester, G. B. Hobbs, A. Teoh, and M. Hobbs. The Australia Telescope National Facility Pulsar Catalogue. *AJ*, 129:1993–2006, April 2005.
- [58] F. Jankowski, W. van Straten, E. F. Keane, M. Bailes, E. Barr, S. Johnston, and M. Kerr. Spectral properties of 441 radio pulsars. *Mon. Not. Roy. Astron. Soc.*, 473(4):4436–4458, 2018.
- [59] A. M. Bykov, E. Amato, A. E. Petrov, A. M. Krassilchtchikov, and K. P. Levenfish. Pulsar wind nebulae with bow shocks: non-thermal radiation and cosmic ray leptons. *Space Sci. Rev.*, 207(1-4):235–290, 2017.
- [60] Pasquale Blasi and Elena Amato. Positrons from pulsar winds. *Astrophysics and Space Science Proceedings*, 21:624, Jan 2011.
- [61] N. Bucciantini, J. Arons, and E. Amato. Modeling the spectral evolution of PWNe inside SNRs. *Mon. Not. Roy. Astron. Soc.*, 410:381, 2011.
- [62] Stefano Gabici, Carmelo Evoli, Daniele Gaggero, Paolo Lipari, Philipp Mertsch, Elena Orlando, Andrew Strong, and Andrea Vittino. The origin of Galactic cosmic rays: challenges to the standard paradigm. 2019.
- [63] E. Cappellaro, R. Evans, and M. Turatto. A new determination of supernova rates and a comparison with indicators for galactic star formation. *A&A*, 351:459–466, Nov 1999.
- [64] Giuseppe Di Bernardo, Carmelo Evoli, Daniele Gaggero, Dario Grasso, and Luca Maccione. Cosmic ray electrons, positrons and the synchrotron emission of the Galaxy: consistent analysis and implications. *Journal of Cosmology and Astro-Particle Physics*, 2013(3):036, Mar 2013.
- [65] Ilias Cholis, Tanvi Karwal, and Marc Kamionkowski. Studying the Milky Way pulsar population with cosmic-ray leptons. *Phys. Rev. D*, 98(6):063008, Sep 2018.
- [66] Pasquale Blasi. The Origin of Galactic Cosmic Rays. *Astron. Astrophys. Rev.*, 21:70, 2013.
- [67] G. Ferrand and S. Safi-Harb. A census of high-energy observations of Galactic supernova remnants. *Advances in Space Research*, 49:1313–1319, May 2012.
- [68] M. A. Malkov and L. O. Drury. Nonlinear theory of diffusive acceleration of particles by shock waves. *Reports on Progress in Physics*, 64:429–481, April 2001.
- [69] D. Caprioli, P. Blasi, E. Amato, and M. Vietri. Dynamical effects of self-generated magnetic fields in cosmic-ray-modified shocks. *The Astrophysical Journal*, 679(2):L139–L142, may 2008.
- [70] V. N. Zirakashvili and V. S. Ptuskin. Acceleration of particles and generation of nonthermal emission in old supernova remnants. *Bulletin of the Russian Academy of Sciences: Physics*, 81(4):434–436, Apr 2017.
- [71] S. J. Schwartz and J. Skilling. The Escape of Cosmic Rays from Supernova Remnants. *A&A*, 70:607, November 1978.
- [72] Stefano Gabici. Cosmic ray escape from supernova remnants. *Mem. Soc. Ast. It.*, 82:760, 2011.
- [73] S. Recchia, S. Gabici, F. A. Aharonian, and J. Vink. A local fading accelerator and the origin of TeV cosmic ray electrons. *arXiv e-prints*, November 2018.
- [74] R. López-Coto, R. D. Parsons, J. A. Hinton, and G. Giacinti. Undiscovered pulsar in the local bubble as an explanation of the local high energy cosmic ray all-electron spectrum. *Phys. Rev. Lett.*, 121:251106, Dec 2018.
- [75] D. Grasso, S. Profumo, A. W. Strong, L. Baldini, R. Bellazzini, E. D. Bloom, J. Bregeon, G. Di Bernardo, D. Gaggero, and N. Giglietto. On possible interpretations of the high energy electron-positron spectrum measured by the Fermi Large Area Telescope. *Astroparticle Physics*, 32(2):140–151, Sep 2009.

- [76] Daniele Gaggero, Fabio Zandanel, Pierre Cristofari, and Stefano Gabici. Time evolution of gamma rays from supernova remnants. *Mon. Not. Roy. Astron. Soc.*, 475(4):5237–5245, 2018.
- [77] R. A. Chevalier. Self-similar solutions for the interaction of stellar ejecta with an external medium. *ApJ*, 258:790–797, Jul 1982.
- [78] Jeremiah P. Ostriker and Christopher F. McKee. Astrophysical blastwaves. *Reviews of Modern Physics*, 60(1):1–68, Jan 1988.